Chapter 3

Hydrodynamic Loading on Vibrating Piezoelectric Microresonators

Huacheng Qiu and Helmut Seidel

Additional information is available at the end of the chapter

http://dx.doi.org/10.5772/intechopen.77731

Abstract

The dynamics of micro-piezoelectric resonators can be profoundly affected by immersion in fluids. Aluminum nitride-based piezoelectric microresonators are fabricated and tested under controlled pressures in several gases. The cases on microresonator vibrating in fluid can be broadly divided into: (i) those that deal with vibration in free space and (ii) close to a surface. For the first case, experimental and analytical results for the hydrodynamic loading characteristics of the resonators at different resonant modes have been investigated, as well as the influences of fluid viscosity and compressibility. For the second case, most prior efforts have been focused on squeeze-film damping with very narrow gaps, while in many practical applications, the resonators vibrate close to a surface with a moderate distance. Experiments by using a micro-bridge resonator with a big range of gaps are performed and compared with predictions from theoretical models.

Keywords: aluminum nitride, fluid-structure interaction, viscous damping, compressibility, wall effect

1. Introduction

Piezoelectric microresonators have been recently used in a large variety of applications [1–9], due to their tiny structures [10] and ultrahigh sensitivity [11], let alone their self-exciting and self-sensing capability, together with full integration, as compared to electrostatic [12], electromagnetic [13], or optically associated [14] structures. Regarding the piezoelectric materials, aluminum nitride (AlN) was selected in this work, to be compatible with complementary metal-oxide-semiconductor (CMOS) technology. Besides, by carefully controlling the fabrication parameters [15], AlN film with high piezoelectric coefficients and low intrinsic stress can be obtained.

Microresonators are normally operated in fluids (such as air or liquid) at atmosphere or under reduced pressure. The resonator parameters, such as resonance frequency f_r, quality factor Q or phase shift, may change due to environmental influences. The Q factor is defined as the ratio of stored energy to the dissipated energy per cycle, equivalents to $f_r/\triangle f$, where $\triangle f$ is the peak width at half power. In general, a high Q factor is preferred for micro-resonator sensors, as high Q factor results in a sharper resonance peak and a better detectable resolution.

The energy loss Q^{-1} for a resonator consists of intrinsic energy loss ${Q_{int}}^{-1}$ (e.g., radiation of elastic energy into attachment and structural friction) [16] and external losses ${Q_{flu}}^{-1}$ (e.g., acoustic, viscous, and squeeze-film damping) into the surrounding fluid. ${Q_{int}}^{-1}$ can be measured by operating the resonator in a high vacuum. When operating in a fluidic environment, ${Q_{flu}}^{-1}$ would be the major energy loss source. The cases on microresonator vibrating in fluid can be broadly divided into (i) those that deal with vibration in free space and (ii) close to a surface. Experimental and analytical results for the hydrodynamic loading characteristics of the resonators in both cases are presented in this chapter.

2. Experimental techniques

In this section, we describe the experimental techniques, including the device fabrication, packaging, measurement setup, and electric readout. Piezoelectric AlN-based resonators were fabricated and tested.

2.1. AlN-based piezoelectric microresonator fabrication

The AlN thin films were deposited using reactive sputtering. Films with good c-axis orientation [15] have been successfully achieved, and the effective piezoelectric constants were measured as: $d_{33} = 3$ pm/V and $d_{31} = -1.0$ pm/V [17].

Low resistivity (less than 0.1 Ω cm) p-type (100) single crystal silicon (SCS) wafer was used as a resonating element, serving simultaneously as a bottom electrode. The fabrication process is shown as in **Figure 1**. The SCS wafer was oxidized in high temperature furnace to form 120 nm thick SiO_2 layers on both sides, and then a 500 nm thick PECVD Si_xN_y layer was deposited on the bottom side of the wafer (**Figure 1a**). In a next step, a 1 μm thick AlN film and a 300 nm thick gold film were deposited on the top side and etched to form a sandwiched piezoelectrode stack (**Figure 1b**). The resonant beam was formed by back side wet etching and then released by a dry etching process (**Figure 1c**). **Figure 2** shows an optical micrograph of a fabricated resonator.

2.2. Device packaging

Two resonator packages were used to investigate the hydrodynamic loading effects in free space or close to a surface. For vibration in free space, the resonator chip was mounted on a printed circuit board, with a pre-drilled hole (c.f. **Figure 3a** and **b**), and the resonator is suspended several millimeters away from any surface, much bigger than the resonator dimensions. For vibration

http://dx.doi.org/10.5772/intechopen.77731

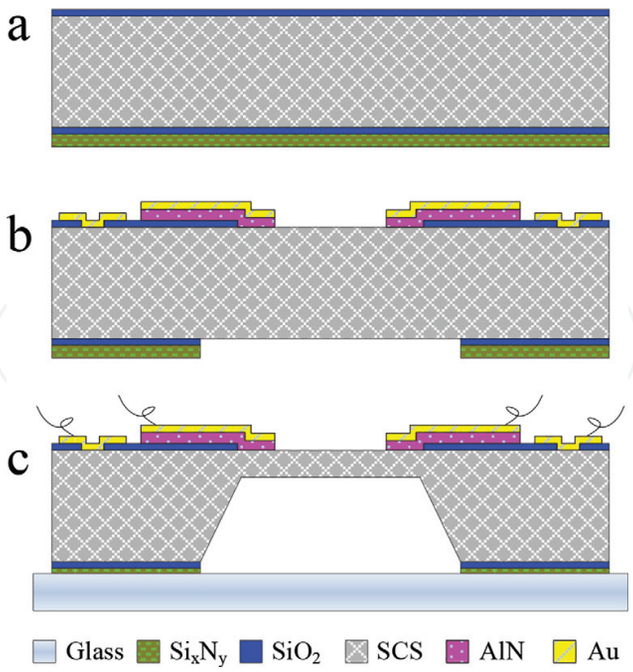

Figure 1. Flow chart of the fabrication process.

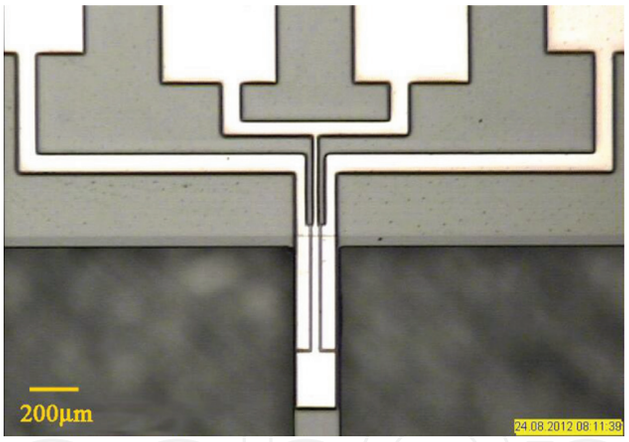

Figure 2. Micrograph of a piezoelectric resonator.

close to a surface, a curved cover was clamped on the top surface of the resonator (c.f. **Figure 3c**, **d**), and the cavity depth h_0 of the cover varies from 20 to 300 μm.

2.3. Measurement setup

The packaged resonator is then mounted on an electronic circuit (whose major functions are electrical crosstalk compensation and signal amplifier, for details one can refer to [18, 19]) and then placed in a custom-built vacuum chamber, wherein the pressure can be controlled from atmospheric pressure down to high vacuum (lower than 10^{-4} mbar). Meanwhile, five noble gases (He, Ne, Ar, Kr, and Xe) and N_2 are used to observe the resonator performance variation.

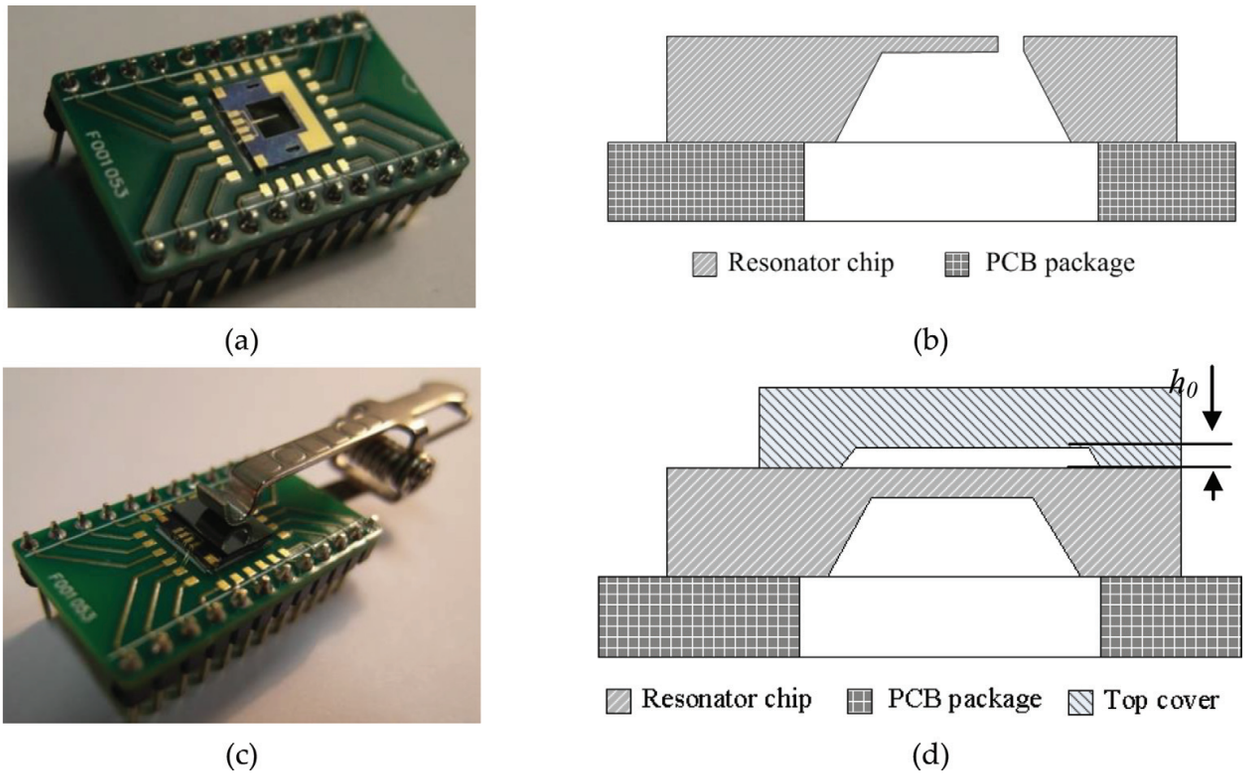

Figure 3. The photos (a and c) and schematic cross-sectional views (b and d) of packaged chips for vibration in free space and close to a surface, respectively.

The noble gases are chosen in this work, since they are all monatomic gases with gradually increasing density and decreasing sound speed under standard conditions. **Figure 4** shows (a) the camera picture (the gas bottles are behind the chamber, not shown in the picture) and (b) the schematic diagram of the measurement setup used to characterize the resonator behavior.

2.4. Electric readout

The resonance frequencies and Q factors of the packaged resonators were measured and characterized under controlled pressures. For vibrations in a high vacuum (10^{-4} mbar), a high Q value can be achieved and the fluidic damping is negligible. Increasing the ambient pressure results in a slight shift in f_r but a dramatic reduction in the Q factor, as shown by example resonant curves in **Figure 5**.

3. Hydrodynamic loading on vibrating microresonators

In this section, the research interest is focused on beam-shaped resonators operating in gas media. First, the full set of Navier-Stokes (N-S) equation is semi-analytically solved, and the solution can be interpreted by a "three wave theory" with coupled viscous, thermal, and acoustic waves. Second, for slender structures at moderate reduced pressures, viscous drag is typically the dominant loss mechanism. The influence of the fluid's viscosity, density, and compressibility on the energy loss of the vibrating beam is discussed. Third, in many practical

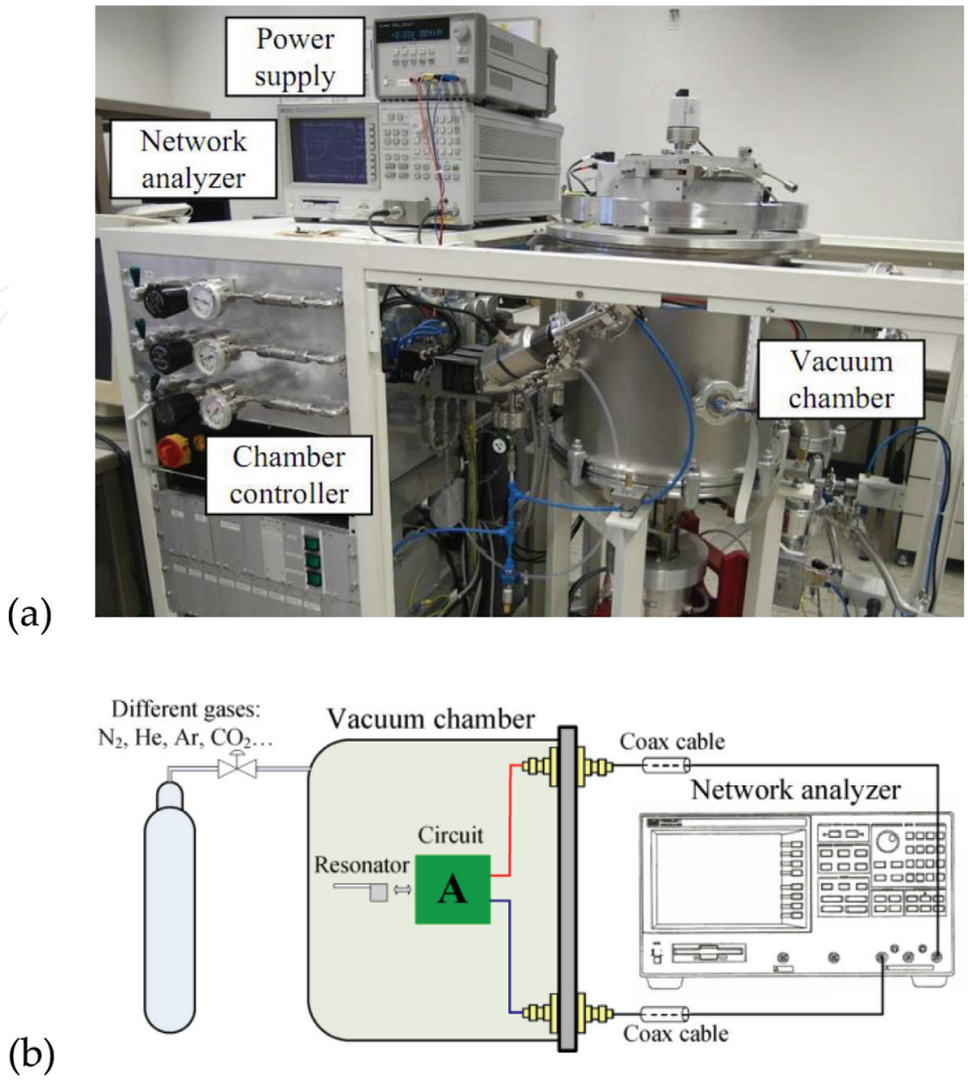

Figure 4. (a) The camera picture and (b) the schematic diagram of the measurement setup used to characterize the microresonators in the vacuum chamber.

applications, resonators are vibrating near a surface, and the influence of the vicinity on such a surface is experimentally and analytically evaluated.

3.1. Full N-S model and numerical simulation

For a continuous fluid, the most extensive type of theoretical model is based on the full set of N-S equations, which takes into account of fluid compressibility, thermal conductivity, and viscosity. The variables are density, pressure, temperature, and velocity that all vary around the resonator.

3.1.1. Theory

The basic equations governing the fluid motion induced by vibration are the compressible N-S equation, the equation of continuity, the equation of state for an ideal gas, and the energy equation [20]. The equations can be written as:

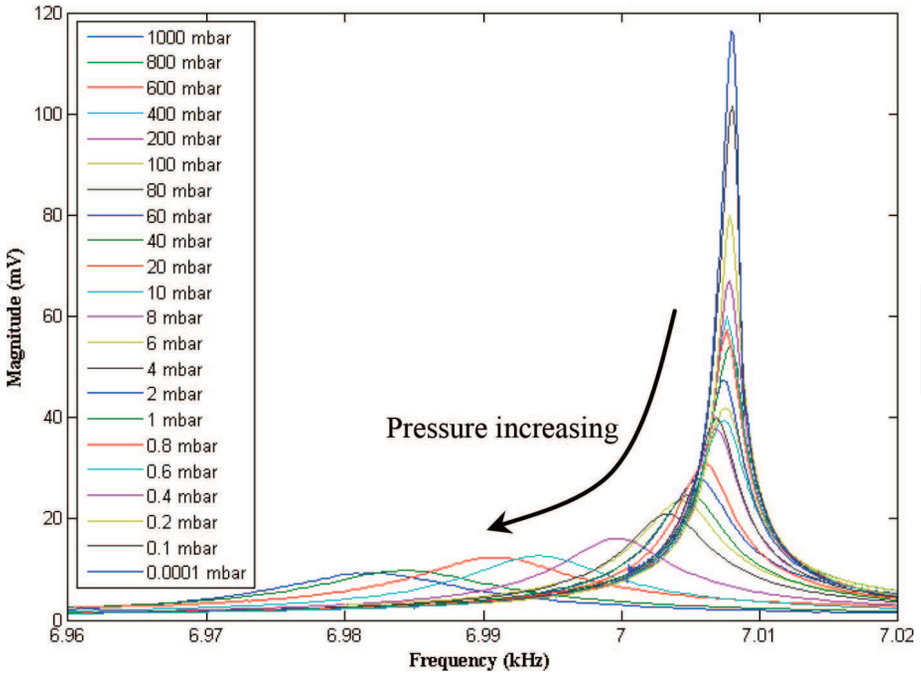

Figure 5. Resonant measurements of a microresonator under the pressures from high vacuum to 1000 mbar in an N_2 environment for the first flexural mode.

$$\partial \mathbf{u}/\partial t + (\mathbf{u} \cdot \nabla)\mathbf{u} = -\frac{1}{\rho}\nabla p + \frac{4}{3}\frac{\eta}{\rho}\nabla(\nabla \cdot \mathbf{u}) - \frac{\eta}{\rho}\nabla \times (\nabla \times \mathbf{u}), \tag{1}$$

$$\rho(\nabla \cdot \mathbf{u}) + \partial\rho/\partial t = 0, \tag{2}$$

$$p = (C_p - C_v)\rho T, \tag{3}$$

$$\rho C_p \partial T/\partial t = \kappa \Delta T + \partial p/\partial t, \tag{4}$$

where $\mathbf{u}$, C_v, and t denote, respectively, the velocity vector, heat capacity at constant volume, and time. The operators ∇ and Δ are the gradient and Laplace operator, respectively.

A solution of the full model called Boundary Element Method (BEM) [21, 22] is discussed here. The velocity is written as the sum of a viscous velocity $\mathbf{u}_v$, due to viscous effects, and a laminar velocity $\mathbf{u}_l$:

$$\mathbf{u} = \mathbf{u}_v + \mathbf{u}_l, \tag{5}$$

which satisfy the conditions that the divergence of the viscous velocity is zero: $\nabla \cdot \mathbf{u}_v = 0$, and the rotation of the laminar velocity is zero: $\nabla \times \mathbf{u}_l = 0$.

The pressure is also split up into two components:

$$p = p_a + p_h, \tag{6}$$

where p_a is the acoustic pressure and p_h is the thermal pressure. Splitting the acoustic variables

http://dx.doi.org/10.5772/intechopen.77731

facilitates rewriting the governing equations into scalar wave equations for the acoustic and thermal pressures and a vector wave equation for the viscous velocity:

$$\left(\Delta + {k_a}^2\right)p_a = 0, \tag{7}$$

$$\left(\Delta + {k_h}^2\right)p_h = 0, \tag{8}$$

$$\left(\Delta + {k_v}^2\right)\mathbf{u}_v = 0. \tag{9}$$

The temperature fluctuation ΔT is the sum of acoustic and thermal temperature variations related to the acoustic and thermal pressures by:

$$\Delta T = \alpha_a p_a + \alpha_h p_h, \tag{10}$$

and the laminar velocity $\mathbf{u}_l$ is written as:

$$\mathbf{u}_l = \phi_a \nabla p_a + \phi_h \nabla p_h. \tag{11}$$

The exact expressions for k_a, k_h, k_v, α_a, α_h, ϕ_a, and ϕ_h can be found in the literatures [21, 22].

3.1.2. Physical interpretation

The solution of the full N-S model can be interpreted as follows: the resonator vibration results in acoustic wave propagation in the ambient fluid. The acoustic domain can be divided into a boundary layer and the bulk region, as illustrated in **Figure 6**. In microscaled geometries, the boundary layer occupies a substantial part of the acoustic domain, the acoustic model needs to account for the viscothermal effects to accurately describe the wave propagation.

Mechel [23] describes the viscothermal acoustic equations as the interaction of viscous, thermal, and acoustic waves. The viscous k_v, thermal k_h, and acoustic k_a wave numbers are derived as: ${k_v}^2 = -i\omega\rho/\eta$, ${k_h}^2 = -i\omega\rho C_p/\kappa$, and $k_a = \omega/c_0$. Viscous and thermal waves are heavily damped, as their wavelengths λ_v and λ_h have comparable length scales with the boundary layer

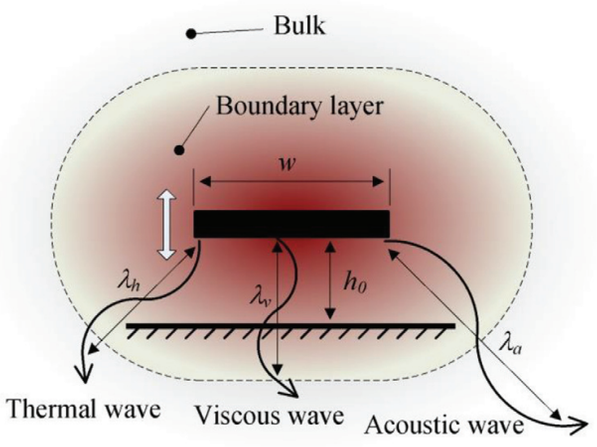

Figure 6. Two regions in the acoustic domain: the bulk and the boundary layer, and three waves due to vibration.

thickness; while the acoustic wave is slightly damped and propagates mainly in the bulk regime. **Figure 7** compares these characteristic length scales for vibration in air at frequencies from 1 kHz to 1 MHz.

For microresonators vibrating at low frequencies, the characteristic length of the resonator (e.g., width of the resonant beam) is much smaller than the acoustic wavelength propagating in the fluid. The acoustic wave develops so weakly that the bulk region can be ignored and the fluid is assumed as incompressible, and the vibration energy is mainly dissipated due to the viscothermal effects. Consequently, the fluid motion can be modeled accurately by incompressible N-S equations. However, as frequency increases, the acoustic wavelength reduces to smaller than the characteristic length of the resonator. The bulk regime can become significant and the acoustic wave starts to radiate vibration energy. Therefore, compressibility can become important for operation at higher frequencies.

3.1.3. Comparison between experiments and simulations

Resonators with different geometry and dimensions have been fabricated to verity the predictions of the full N-S model. One of the AlN-based resonators is shown in **Figure 8**, the insert shows the resonator chip mounted on a printed circuit board. The resonator has been tested from high vacuum to normal atmosphere.

The full model equations are solved and simulated with a self-developed FEM solver using MATLAB. **Figure 9** shows the simulated pressure, density, temperature, and velocity amplitude distributions of the air gap in the *xz* plane at 0.01 and 1000 mbar. The amplitude profiles in **Figure 9** indicate that, compare to vibration in the higher pressure, the pressure and density perturbation are more constant, and the temperature is more homogenous across the air gap in the lower pressure.

The measured and simulated air damping coefficients under different pressures are shown in **Figure 10**. This figure indicates that simplified models, such as viscous model or squeeze model, are not suitable in this case, since they are accurate only for resonators with slim beams

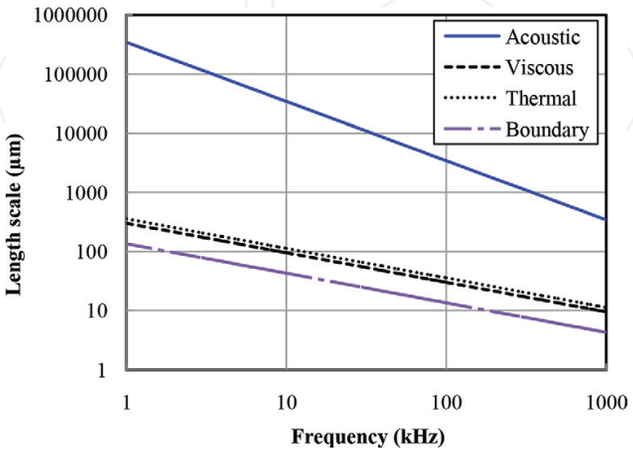

Figure 7. Characteristic length scales for vibrations in air: acoustic (solid), viscous (dashed), thermal (dotted) wavelengths, and boundary layer thickness (dash-dotted).

http://dx.doi.org/10.5772/intechopen.77731

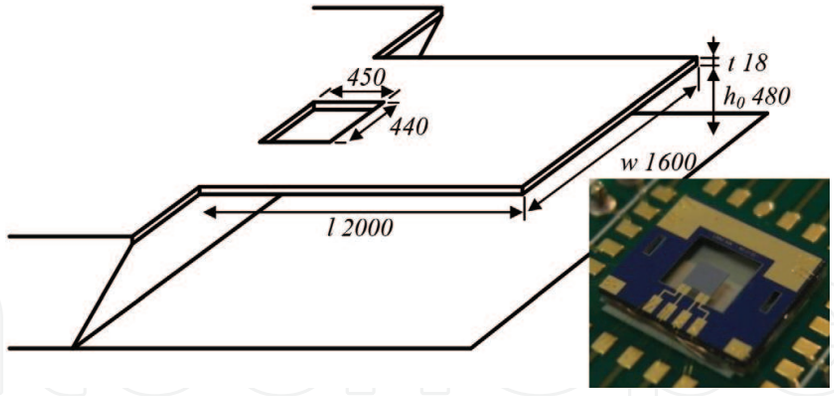

Figure 8. The geometry of the resonator (in μm). The insert shows the photo of the resonator [24].

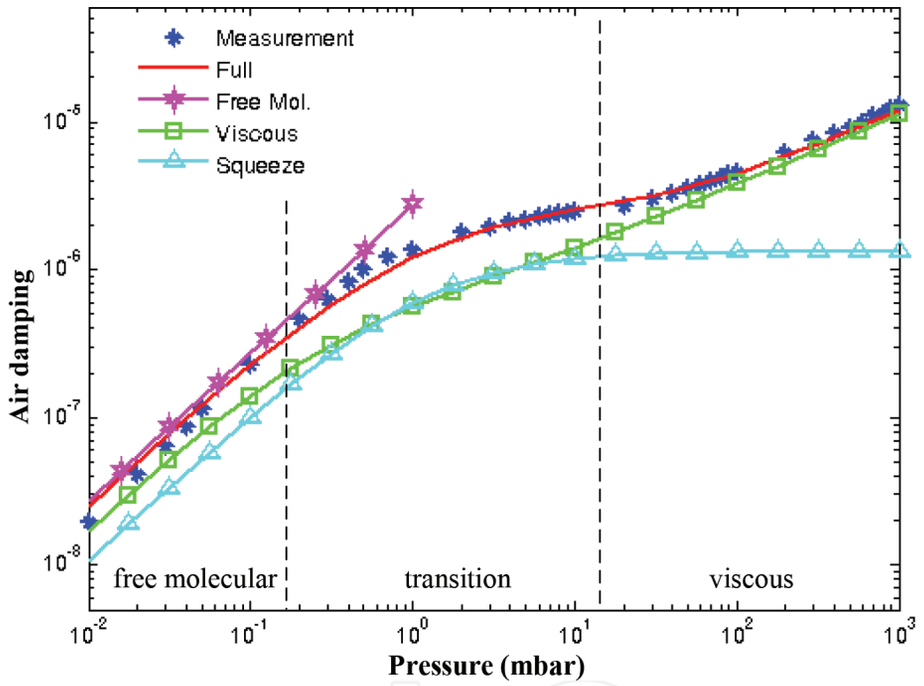

Figure 9. Amplitude profiles of (a) pressure, (b) density, (c) temperature, and (d) velocity in the air gap at 0.01 mbar (column I) and at 1000 mbar (column II) [24].

or narrow air gaps. In the free molecular region, the free molecular model is reasonable. The full N-S model yields good agreement in the whole pressure range.

3.2. Hydrodynamics of microresonators vibrating in unbounded fluids

3.2.1. Measurement results at atmospheric pressure

The AlN-based microresonators were tested in the chamber filled with different gases under atmospheric pressure, as shown in **Figure 11**. The resonance curve variations indicate that the resonance frequency f_r decreases as the density of the gas increases, shifting from 7 kHz for He (ρ = 0.18 kg/m^3) to 6.91 kHz for Xe (ρ = 5.90 kg/m^3).

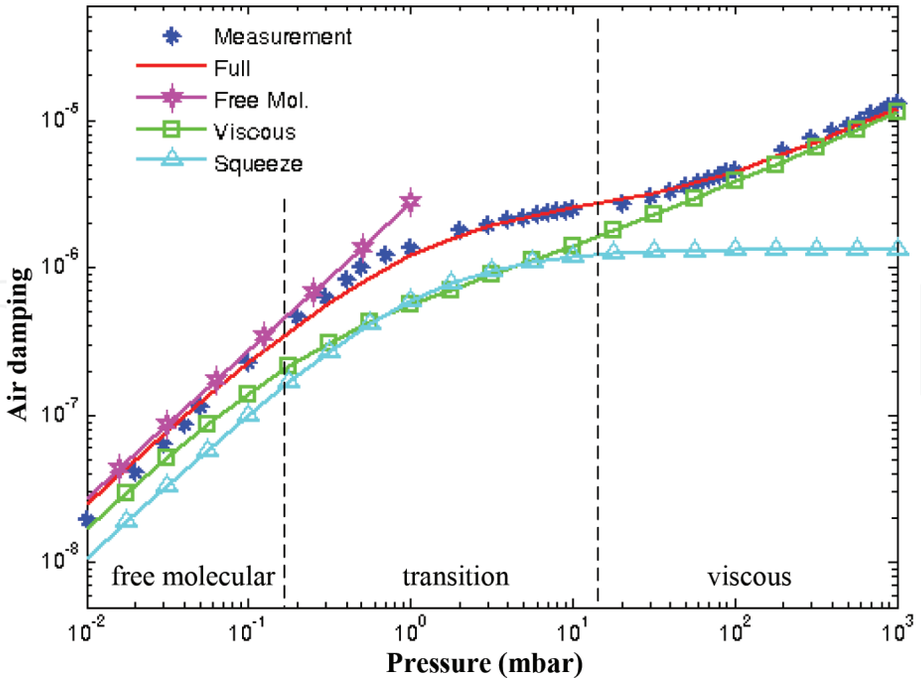

Figure 10. Air damping coefficient of the resonator as a function of ambient pressure [24].

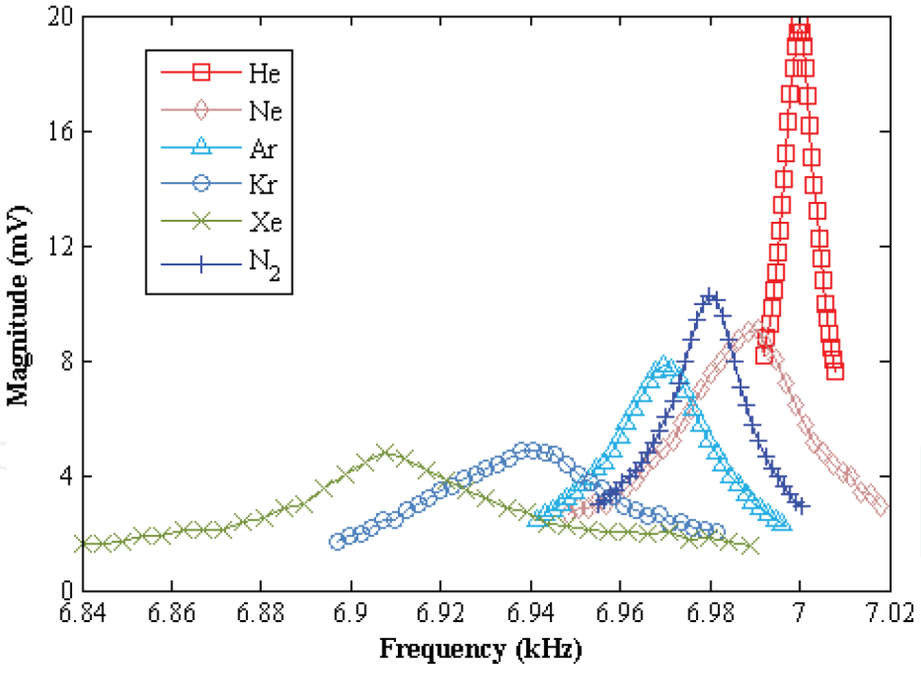

Figure 11. Resonant measurements of the cantilever with different gases at atmospheric pressure in its first flexural mode [25].

To excite the cantilever in higher resonant modes, the frequency of the driving voltage was scanned from 5 to 250 kHz. **Figure 12** shows the resonance frequency response of the cantilever in N_2 at atmospheric pressure. Finite element analysis software COMSOL was used to assign the resonant modes to the observed peaks. The resonant mode shapes inserted in the figure are obtained by this software and depict the displacement of the cantilever for each mode.

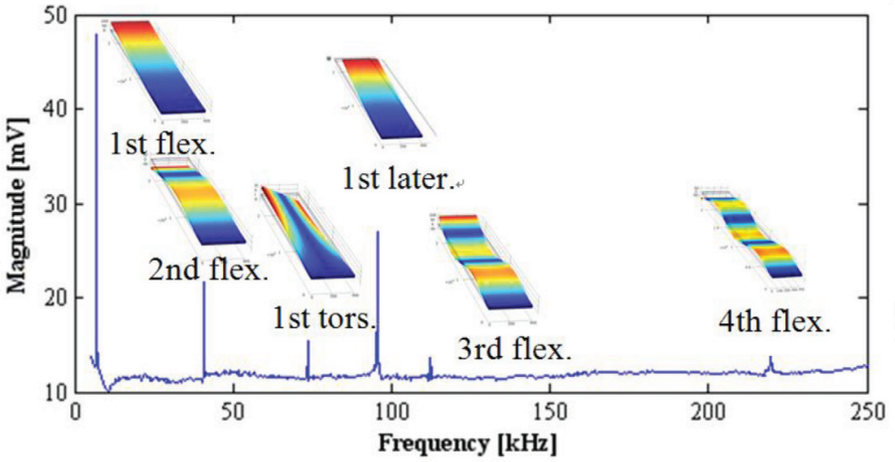

Figure 12. Amplitude spectrum and mode shapes of the cantilever at normal atmospheric N_2 [25].

To evaluate the fluidic hydrodynamic loading effects, the cantilever vibrating in different resonant modes has been characterized in different gases at atmospheric pressure. Only the first two modes for Kr and Xe could be detected, since the signal of higher modes was too weak. The remaining gases are successfully characterized up to the fourth flexural mode. Pure fluidic hydrodynamic loading is evaluated by subtracting the intrinsic damping, which can be measured in a high vacuum.

The quality factor induced by gas damping Q_{gas} in atmospheric pressure is characterized and illustrated in **Figure 13**. Resonator immersed in He shows the highest Q factors for all modes. The two lightest gases, He and Ne, exhibit a continuous increase in Q_{gas} with the mode number, whereas for Ar and N_2, Q_{gas} decreases beyond the third mode. Taking N_2 as an example, the measured values of Q_{gas} increase from 543 to 1890 for the first to third

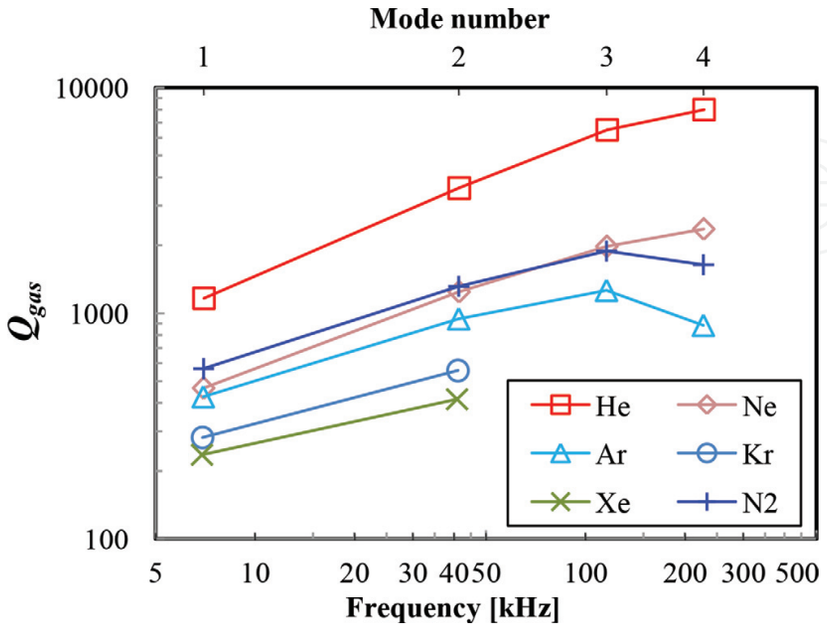

Figure 13. Q factors due to gas damping of the different flexural modes at atmospheric pressure [25].

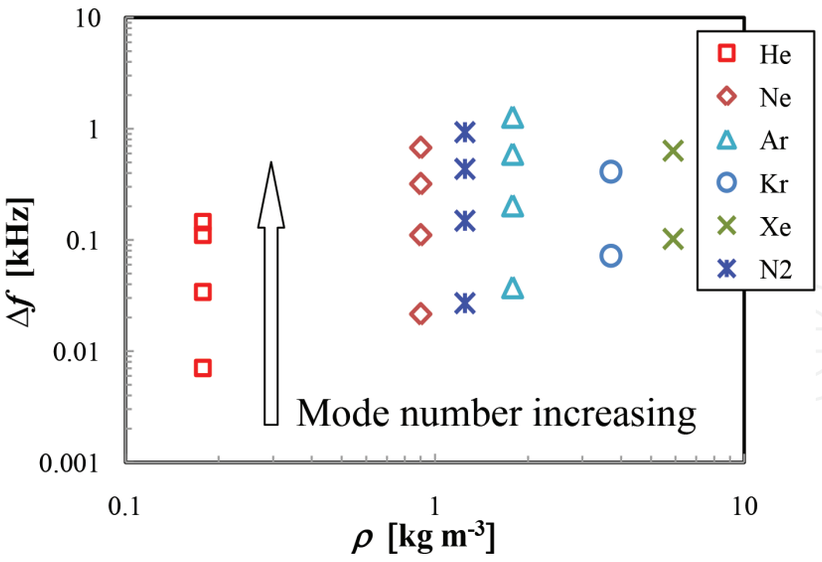

Figure 14. Resonance frequency shifts Δf of the different flexural modes at atmospheric pressure [25].

modes. However, this trend is broken when Q_{gas} reduces to 1645 for the fourth flexural mode, indicating that Q_{gas} will not increase in an unlimited way with increasing mode/frequency.

The corresponding resonance frequency shift Δf, defined as $f_{r,vac} - f_r$, where $f_{r,vac}$ corresponds to the resonance frequency f_r in vacuum, has been characterized. **Figure 14** shows Δf as a function of density ρ for different gases. The results in this figure indicate a dependence on both f_r and ρ.

3.2.2. Measured results at reduced pressures

The resonators were further tested at reduced pressures to investigate the influence of ambient pressure. **Figure 15** shows the measured Q factor curve of one resonator vibrating at the first flexural mode as a function of N_2 pressure. When the pressure is sufficiently low ($<10^{-3}$ mbar in this figure), the damping is independent of the fluid and relates only with intrinsic losses in the resonator structure. Consequently, this pressure regime is called the intrinsic regime. Gas damping starts to become visible at higher pressure levels. Three regions can be identified by using the Knudsen number Kn (defined as the ratio between the mean free path of the fluid and the width of the resonator):

- The molecular regime ($Kn > 10$): damping is caused by independent collisions of non-interacting fluid molecules with the vibrating surface of the resonator and/or surrounding walls.
- The transition regime ($0.01 < Kn < 10$): the fluid is neither noninteracting nor continuous.
- The continuous regime ($Kn < 0.01$): the fluid acts as continuum and most previous papers (e.g., [26, 27]) found that the viscous drag is typically the dominant energy loss mechanism based on the incompressible gas assumption.

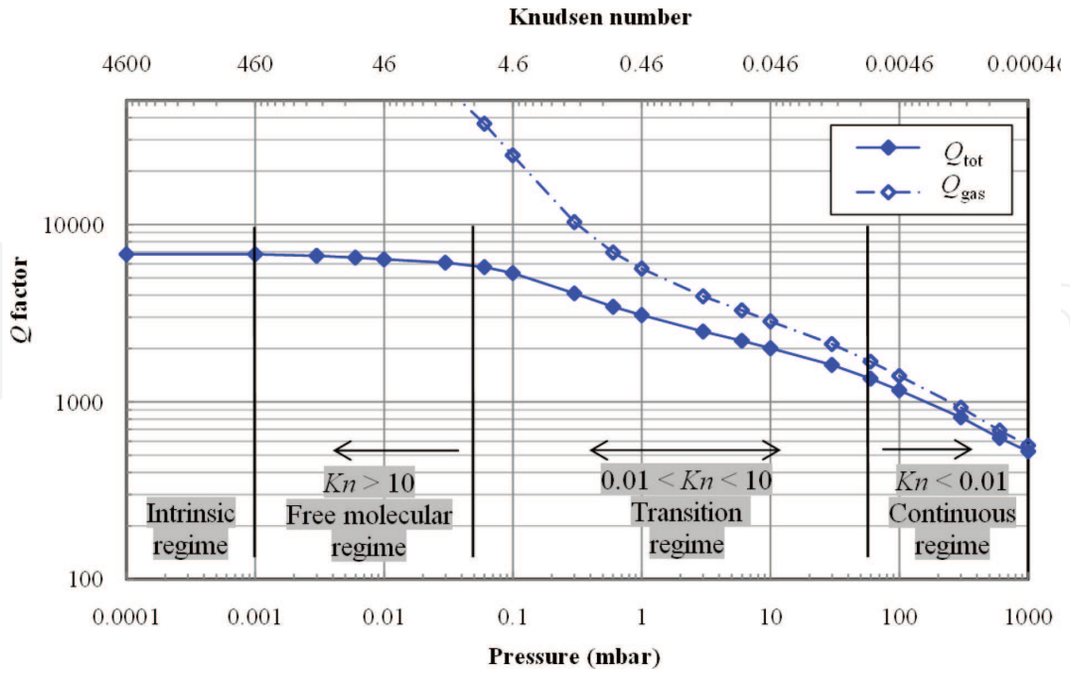

Figure 15. Variation of the Q factor with N_2 pressure. The solid diamond points are the measurements, while the hollow points are the derived Q factors due to fluidic damping.

3.2.3. Results analysis

It is found that the fluidic loading has a strong effect on the resonant behavior of the resonator, especially at higher pressures (e.g., near atmospheric pressure). The following analysis focuses on fluidic damping at atmospheric pressure, which is commonly present in many practical applications.

Viscous drag is typically the dominant loss mechanism, for most microdevices vibrating at relatively low frequency. For a microcantilever with dimensions of length l, width w, and thickness h, undergoing flexural vibrations in a continuous incompressible fluid, the corresponding Q factor due to viscous damping is given by [25, 28, 29]:

$$Q_{vis} \approx \frac{\rho_b h}{\sqrt{\pi}} \sqrt{\frac{f_r}{\rho \eta}}, \tag{12}$$

where ρ_b is the cantilever beam density. It can be seen that the Q factor scales inversely proportional with $\sqrt{\rho\eta}$ and proportional with $\sqrt{f_r}$, which means that a higher resonance frequency (or higher resonant mode) results in a higher Q factor. The measured and calculated Q factors Q_{gas} of the different flexural modes are plotted in **Figure 16** as a function of the combination of the resonance frequency f_r, the density ρ, and the viscosity η of the surrounding gases. However, as noted before, a decrease of the quality factor is observed for the third and fourth modes of Ar and N_2.

One possible reason is the additional acoustic damping due to the compression of the fluid. Incompressible flow is expected for low frequency vibrations, since the wavelength of sound in the fluid is much longer than the dominant length scale of the vibrating beam. As the resonant mode increases, the acoustic wavelength reduces and the incompressible gas assumption is no

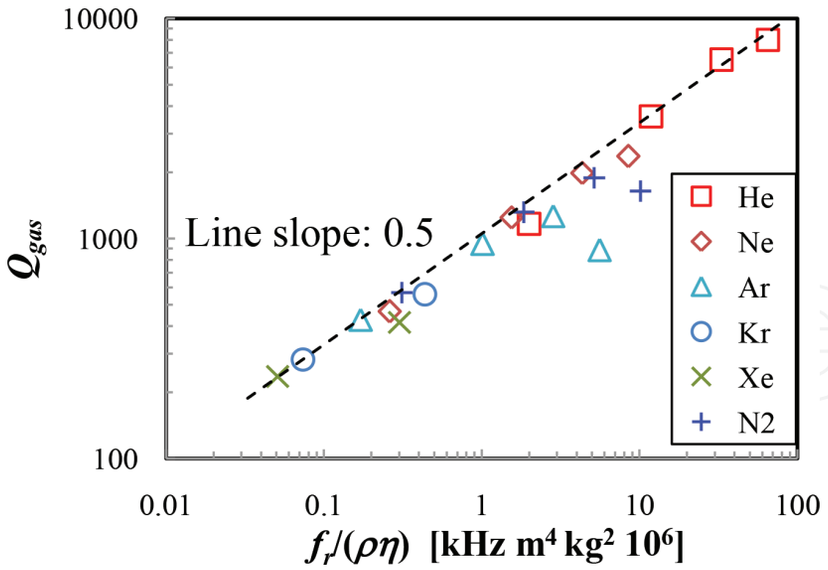

Figure 16. Evolution of the Q factors as a function of $f_r/(\rho\eta)$ for different gases and resonant modes at atmospheric pressure. The dashed line represents the viscous model (Eq. (1)) prediction [25].

longer valid [25, 29, 30]. Thus, at high frequencies, acoustic energy loss becomes important in addition to viscous loss.

3.3. Hydrodynamics of microresonators vibrating close to a surface

3.3.1. Measured results

We have measured bridge resonator different gap depths to understand how fluidic hydrodynamic load is modified when the resonator is vibrating near a surface. The case of vibration at free space was also measured for comparison. We begin by presenting results of the resonance responses of the resonator immersed in atmospheric N_2 at room temperature, as shown in **Figure 17**.

It is obvious that the air gap has a strong effect on the resonance behavior. A general trend is the resonance peak getting broaden and shifting to lower peak frequency as the gap depth decreases. There results fit with the expectation that the fluidic damping increases significantly when approaching toward a surface. We have also observed that the resonance frequency shift is relatively insensitive to air gap when the separation h_0 is bigger than 150 μm, which corresponds to a gap to the resonator width ratio of more than 0.5. However, for h_0 = 150 μm, the Q factor is approximately 20% less than vibration without gap, and for h_0 = 250 μm, the Q factor differs by only less than 2%.

To quantify the pressure effect on the dissipation in the fluid as the resonator is vibrating near a surface, it was further measured under reduced pressures. **Figure 18** shows the quality factors for different gap heights and pressures in N_2 atmosphere.

3.3.2. Review of analytical models

In many practical applications, restrictive squeeze-film assumption (very narrow air gap) does not always hold; thus, traditional squeeze-film models are not suitable in those cases. Two

http://dx.doi.org/10.5772/intechopen.77731

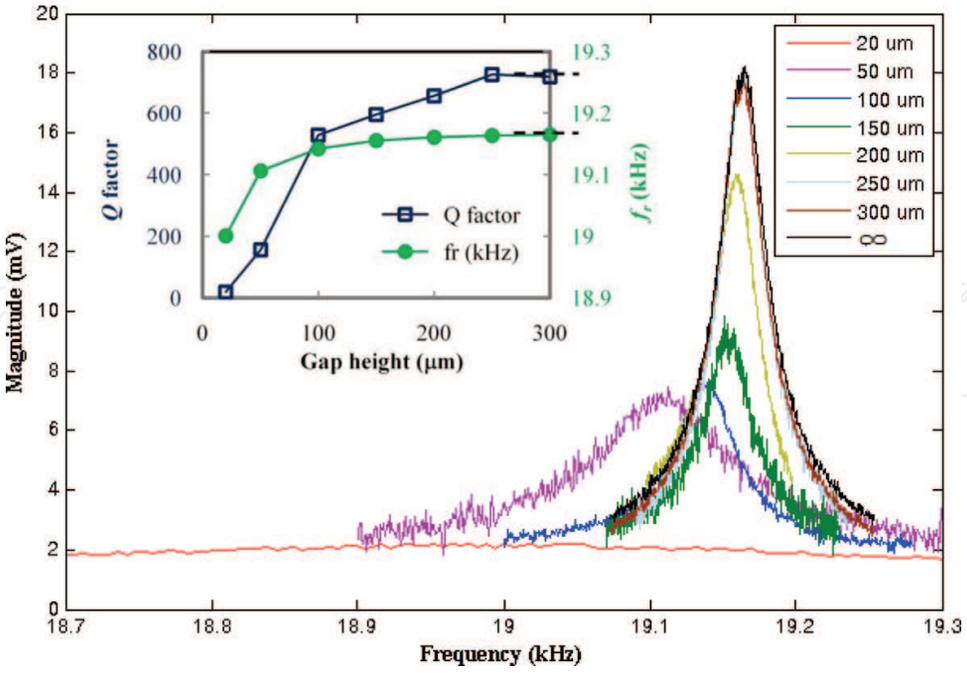

Figure 17. Resonant curves of a bridge resonator in fundamental mode at atmospheric N_2. The curves for gap depths of 250 and 300 μm and ∞ are overlapped. The dashed lines in the inserted figure represent the limit for the resonator at free space [31].

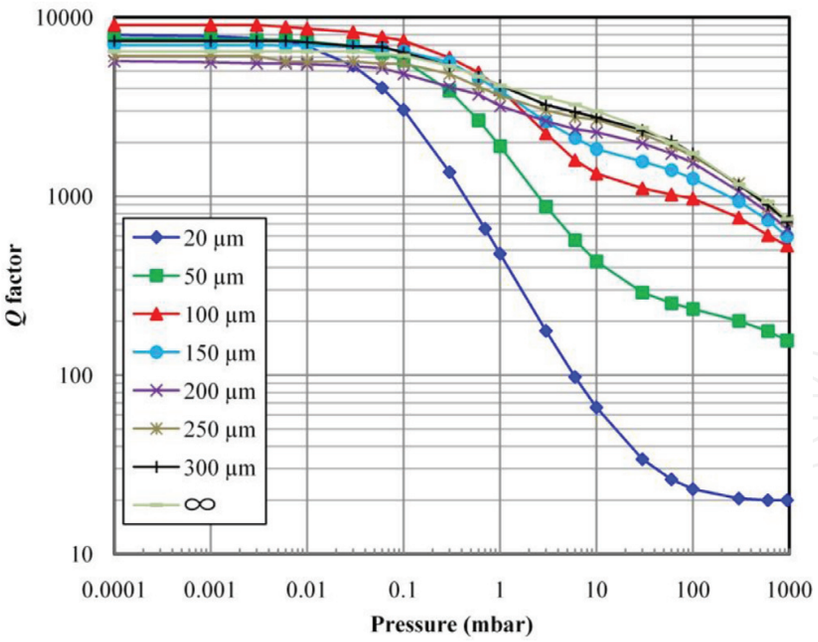

Figure 18. Variation of Q factors with ambient pressure for N_2 with different gap heights [31].

recently improved models, namely (a) extended squeeze-film model [32, 33] and (b) unsteady N-S model [34–36], are considered for describing the behavior of the resonators with moderate gap depths.

3.3.2.1. Extended squeeze-film model

Osborne Reynolds first formulated the theory for a squeezed film between two surfaces in relative motion to each other more than a century ago [37]. Generally, the compressibility should be considered and its importance increases as vibration frequency. An important measure for the squeezed-film effect is the squeeze number:

$$\sigma = \frac{12\eta w^2 \omega}{p{h_0}^2}, \tag{13}$$

where η is the fluid viscosity, ω is the angular frequency of the resonator, p is the ambient pressure, w is the width of the resonator, and h_0 is the gap depth. The number σ specifies the ratio between the spring force due to the gas compressibility and the force due to the viscous flow. When σ is much smaller than 1, the gas in the film has enough time to "leak" out; thus, the gas is referred to as incompressible. For the resonator geometry in this study, the resonator width w and the gap depth h_0 are of the same order, e.g., $h_0/w > 0.05$. For air at atmospheric pressures, the vibrating frequency should be higher than 150 kHz to ensure σ is bigger than 1.

When σ is very small, the compressible effects can be ignored and the damping coefficient for a slender resonator can be written as:

$$c = \frac{\eta l w^3}{{h_0}^3}, \tag{14}$$

and Q factor is then given by:

$$Q = \frac{\rho_b t \omega}{\eta w^2} {h_0}^3, \tag{15}$$

herein ρ_b, l and, t are the density, length, and thickness of the resonator, respectively.

An effective plate width $w_{eff} = w + \Delta w$ is introduced, to include border effects into the much simplified squeeze-film model. The effective width is such that the damping force for the enlarged plate with trivial boundary conditions has the same values as that of a real device size with the border effects. This concept is illustrated in **Figure 19**.

One method to predict the elongation caused by the border effect was proposed by Veijola et al. [32, 33], based on a series of 2D and 3D FEM simulations. A simple conclusion has been obtained for a slender beam:

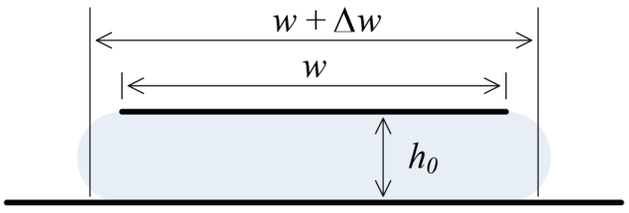

Figure 19. Schematic diagram of extended squeeze-film model.

$$\Delta w = 1.3h_0. \tag{16}$$

The fluidic damping coefficient due to air gap is:

$$c = \frac{\eta l(w + 1.3h_0)^3}{{h_0}^3}. \tag{17}$$

The quality factor consequently is:

$$Q = \frac{\rho_b wt\omega}{\eta(w + 1.3h_0)^3}{h_0}^3. \tag{18}$$

To account the non-continuum fluid behavior at very low pressures or for a narrow gap, an effective viscosity η_{eff} is used instead of the gas dynamic viscosity η. Burgdoufer [38] obtained a simple form for the effective viscosity coefficient:

$$\eta_{eff} = \frac{\eta}{1 + 6K_n}. \tag{19}$$

3.3.2.2. Unsteady N-S model

Another method to deal with moderate gaps can be based on the unsteady incompressible N-S equation and the continuity equation [20]. For a beam undergoing normal oscillations in a viscous fluid, the general form of the hydrodynamic force in the vibration direction is given as [39]:

$$\mathbf{F_d} = \frac{\pi}{4}\rho\omega^2 w^2 l\Gamma(Re)\hat{W}(x|\omega), \tag{20}$$

where ρ is the fluid density, $\hat{W}$ is the Fourier transformation of the resonator beam deformation. Γ, the so-called "hydrodynamic function", is a complex term: the real part Γ_{real} represents the inertial forces of the fluid or added mass components, whereas the imaginary part Γ_{imag} is proportional to the viscous forces of the fluid or damping components.

The general form of the semi-analytical formula for the hydrodynamic function is $\Gamma(Re, H) = 10^{\Gamma_L}$ where

$$\begin{aligned}\Gamma_L(Re, H_L) = {} & a_1 + a_2 Re_L + a_3 {Re_L}^2 + a_4 {Re_L}^3 + a_5 {Re_L}^4 \\ & + a_6 Re_L H_L + a_7 H_L + a_8 {H_L}^2 + a_9 {H_L}^3 + a_{10} {H_L}^4 \\ & + a_{11} Re_L H^L L^2 + a_{12} {Re_L}^2 H_L + a_{13} Re_L {H_L}^3 + a_{14} {Re_L}^3 H_L \\ & + a_{15}(Re_L H_L)^2 + a_{16}(Re_L H_L)^3,\end{aligned} \tag{21}$$

$H_L = \log_{10}(H)$, and $Re_L = \log_{10}(Re)$. The coefficients a_k, k = 1, 2, …, 16, have complex values. They are tabulated in Tung et al.'s paper [36]. The fit is valid in the range of $10^{-2} < Re < 10^4$ and $10^{-1} < H < 10$. The Q factor due to the fluid damping is defined by

$$Q = \frac{4\rho_b t}{\pi \rho w \Gamma_{imag}}. \tag{22}$$

The calculations are technically valid only when the continuum hypothesis holds. This is because the theory is based upon a subset of the N-S equations, which are based on a continuum assumption. The useful range of this semi-analytical expression can be extended beyond the continuum regime and into the slip and transition regimes by using an effective viscosity concept.

3.3.3. Results analysis

The predictions from squeeze film (Eq. (13)), extended squeeze film (Eq. (18)), unsteady N-S (Eq. (22)), and viscous (Eq. (12)) models are compared with the experimental data. **Figure 20** shows the results for the first flexural mode of the bridge resonator oscillating in atmospheric N_2 with different gap depths. The intrinsic damping of the resonator can be obtained by operating in a high vacuum, and this damping was subsequently removed mathematically, leaving only the fluidic damping to be analyzed.

The traditional squeeze-film damping model overestimates the Q factor and the divergence increases rapidly as the gap depth increases. While the extended squeeze-film model predicts well the squeeze-film damping up to gap depth of 50 μm. This model accurately predicts the fluidic damping well even into the free molecular regime, indicating the "effective viscosity" concept is reasonable to account the rarefaction effect of the gas in a narrow gap. The unsteady N-S model predictions are in better agreement with measurements as compared to other models. The viscous model fits well with the measurements in the viscous regime, but when the pressure decreases into the transition regime, this model loses its validity.

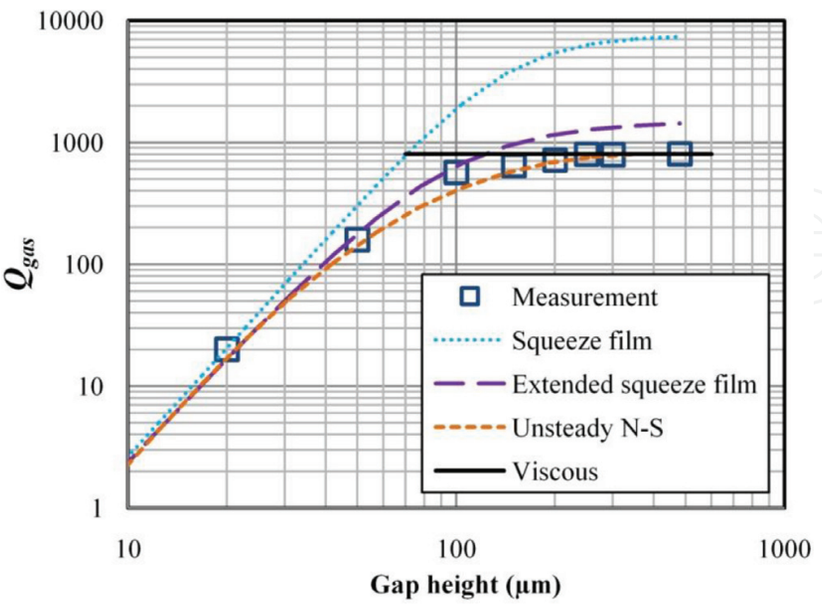

Figure 20. Q factors due to fluidic damping of a resonator. The squares represent the measurements, and the dashed lines represent the analytical/semianalytical calculations, while the solid line shows the viscous model prediction [31].

4. Conclusion and discussion

In this work, AlN-based piezoelectric microresonators have been fabricated and measured to study the fluidic hydrodynamic loading mechanisms. Experimental, computational, and analytical tools have been developed, to analyze the dynamics of the resonators in different gases from atmospheric pressure to high vacuum.

For resonators vibrating in a continuous fluid, the extensive type of theoretical model is based on the full set of N-S equations. The equations were semi-analytically solved using the BEM method. The solution can be interpreted as coupling of viscous, thermal, and acoustic waves. However, this method does have some disadvantages, such as being computationally costly, relying on sophisticated numerical techniques, and being non-intuitive with respect to understand the results physically.

The resonators vibrating in free space fluids have been investigated, by measuring microcantilevers in different gases and explaining the results using simplified models based on the incompressible N-S equation. The analytical models agree reasonably with measurements. Besides, it is found that the compressibility of gases leads to additional acoustic damping when vibrating in higher mode/frequency.

For vibration close to a surface, experiments were performed using a bridge resonator with a big range of gap depths. The traditional squeeze-film model could predict the squeeze-film damping when the ratio of the resonator width to gap height w/h_0 was bigger than 10, and the gas rarefaction effect in the gap can be accounted by using an "effective viscosity" concept. The extended squeeze-film model was valid for $w/h_0 \geq 4$. The unsteady N-S model could be used when the gap height was even bigger.

Author details

Huacheng Qiu[1]* and Helmut Seidel[2]

*Address all correspondence to: huacheng.qiu@outlook.com

1 China Aerodynamics Research and Development Center, Hypervelocity Aerodynamics Institute, Sichuan Province, China

2 Saarland University, Chair of Micromechanics, Microfluidics/Microactuators, Saarbrücken, Germany

References

[1] Ruby R. Review and comparison of bulk acoustic wave FBAR, SMR technology. In: Proc. IEEE Ultrasonic Symposium. 2007. pp. 1029-1040

[2] Martin PM, Good MS, Johnston JW, Posakony GJ, Bond LJ, Crawford SL. Piezoelectric films for 100-Mhz ultrasonic transducers. Thin Solid Films. 2000;**379**:253-258

[3] Madni AM, Costlow LE, Knowles SJ. Common design techniques for BEI GyroChip quartz rate sensors for both automotive and aerospace/defense markets. IEEE Sensors Journal. 2003;**3**:569-578

[4] Beeby SP, Ross JN, White NM. Design and fabrication of a micromachined silicon accelerometer with thick-film printed PZT sensor. Journal of Micromechanics and Microengineering. 2000;**10**:322-328

[5] Stephanou PJ, Piazza G, White CD, Wijesundara MBJ, Pisano AP. Piezoelectric aluminum nitride MEMS annular dual contour mode filters. Sensors and Actuators A. 2007;**134**:152-160

[6] Horowitz SB, Sheplak M, Cattafesta LN, Nishida T. A MEMS acoustic energy harvester. Journal of Micromechanics and Microengineering. 2006;**16**:174-181

[7] Sökmen Ü, Stranz A, Waag A, Ababneh A, Seidel H, Schmid U, Peiner E. Evaluation of resonating Si cantilevers sputter-deposited with AlN piezoelectric thin films for mass sensing applications. Journal of Micromechanics and Microengineering. 2010;**20**:064007

[8] Ayela C, Nicu L. Micromachined piezoelectric membranes with high nominal quality factors in Newtonian fluid media: A lamb's model validation at the microscale. Sensors and Actuators B: Chemical. 2007;**123**:860-868

[9] James D, Scott SM, Ali Z, O'Hare WT. Chemical sensors for electronic nose systems. Microchimica Acta. 2005;**149**:1-17

[10] Waggoner PS, Craighead HG. Micro- and nanomechanical sensors for environmental, chemical, and biological detection. Lab on a Chip. 2007;**7**:1238-1255

[11] Fadel L, Lochon F, Dufour I, Français O. Chemical sensing: Millimeter size resonant microcantilever performance. Journal of Micromechanics and Microengineering. 2004;**14**:S23

[12] Kim SJ, Ono T, Esashi M. Study on the noise of silicon capacitive resonant mass sensors in ambient atmosphere. Journal of Applied Physics. 2007;**102**:104304

[13] Xia X, Zhang Z, Li X. A Latin-cross-shaped integrated resonant cantilever with second torsion-mode resonance for ultra-resoluble bio-mass sensing. Journal of Micromechanics and Microengineering. 2008;**18**:035028

[14] Zhou J, Li P, Zhang S, Huang Y, Yang P, Bao M, Ruan G. Self-excited piezoelectric microcantilever for gas detection. Microelectronic Engineering. 2003;**69**:37-46

[15] Ababneh A, Schmid U, Hernando J, Sánchez-Rojas JL, Seidel H. The influence of sputter deposition parameters on piezoelectric and mechanical properties of AlN thin films. Materials Science and Engineering B. 2010;**172**:253-258

[16] Qiu HC, Ababneh A, Feili D, Wu XZ, Seidel H. Analysis of intrinsic damping in vibrating piezoelectric microcantilevers. Microsystem Technologies. 2016;**22**(8):2017-2025

[17] Hernando J, Sánchez-Rojas JL, González-Castilla S, Iborra E, Ababneh A, Schmid U. Simulation and laser vibrometry characterization of piezoelectric AlN thin fims. Journal of Applied Physics. 2008;**104**:053502

[18] Qiu HC, Schwarz P, Feili D, Merzsh S, Peiner E, Wu XZ, Seidel H. Electrical performance analysis and characterization of two port piezoelectric resonators. Microsystem Technologies. 2013;**19**:1131-1136

[19] Qiu HC, Schwarz P, Völlm H, Feili D, Wu XZ, Seidel H. Electrical crosstalk in two-port piezoelectric resonators and compensation solutions. Journal of Micromechanics and Microengineering. 2013;**23**:045007

[20] Landau LD, Lifshitz EM. Fluid Mechanics. 2nd ed. Oxford: Pergamon Press; 2004

[21] Beltman WM. Viscothermal wave propagation including acousto-elastic interaction, part I. Theory. Journal of Sound and Vibration. 1999;**227**:555-586

[22] Beltman WM. Viscothermal wave propagation including acousto-elastic interaction, part II. Applications. Journal of Sound and Vibration. 1999;**227**:587-609

[23] Mechel FP. Revision of the Kirchhoff-Rayleigh theory of sound propagation in viscothermal air. Acta Acustica United with Acustica. 2007;**93**:507-534

[24] Qiu HC, Schwarz P, Feili D, Wu XZ, Seidel H. Viscothermal acoustic waves in micro scale resonators. In: Proceedings of Transducers 2013 & Eurosensors XXVII. 2013. 1719-1722

[25] Qiu HC, Xiao DB, Feili D, Wu XZ, Seidel H. Hydrodynamic analysis of piezoelectric microcantilevers vibrating in viscous compressible gases. Sensors and Actuators A. 2016; **238**:299-306

[26] Johnson BN, Mutharasan R. Dependence of the quality factor of micromachined silicon beam resonators on pressure and geometry. Journal of Vacuum Science and Technology B. 1992;**10**:19-26

[27] Bhiladvala RB, Wang ZJ. Effect of fluids on the *Q* factor and resonance frequency of oscillating micrometer and nanometer scale beams. Physical Review E. 2004;**69**:036307

[28] Blom FR, Bouwstra S, Elwenspoek M, Fluitman JHJ. Dependence of the *Q* factor of micromachined silicon beam resonators on pressure and geometry. Journal of Vacuum Science and Technology. 1992;**10**:19-26

[29] Qiu HC, Feili D, Wu XZ, Seidel H. Resonant-mode effect on fluidic damping of piezoelectric microcantilevers vibrating in an infinite viscous fluid. Sensors and Actuators A. 2014; **232**:1-7

[30] Van Eysden CA, Sader JE. Compressible viscous flows generated by oscillating flexible cylinders. Physics of Fluids. 2009;**21**:013104

[31] Qiu HC, Schwarz P, Feili D, Wu XZ, Seidel H. Hydrodynamics of micro beam resonator vibrating close to a surface with a moderate distance. Journal of Micromechanics and Microengineering. 2014;**25**:055016

[32] Veijola T, Pursula A, Raback P. Extending the validity of existing squeeze-film damper models with elongations of surface dimensions. In: Proc. Nanotech 2004. 2004. pp. 235-238

[33] Veijola T, Pursula A, Raback P. Extending the validity of squeeze-film damper models with elongations of surface dimensions. Journal of Micromechanics and Microengineering. 2005; **15**:1624-1636

[34] Green CP, Sader JE. Frequency response of cantilever beams immersed in viscous fluids near a solid surface with applications to the atomic force microscope. Journal of Applied Physics. 2005;**98**:114916

[35] Green CP, Sader JE. Small amplitude oscillations of a thin beam immersed in a viscous fluid near a solid surface. Physics of Fluids. 2005;**17**:073102

[36] Tung RC, Jana A, Raman A. Hydrodynamic loading of microcantilevers oscillating near rigid walls. Journal of Applied Physics. 2008;**104**:114905

[37] Langlois WE. Isothermal squeeze films. Quarterly of Applied Mathematics. 1962;**XX**(2): 131-150

[38] Burgdorfer A. The influence of the molecular mean free path on the performance of hydrodynamic gas lubricated bearings. Journal of Basic Engineering. 1959;**81**:94-99

[39] Sader JE. Frequency response of cantilever beams immersed in viscous fluids with applications to the atomic force microscope. Journal of Applied Physics. 1998;**84**:64-76